Retained austenite-aided cyclic plasticity of the quenched 9Ni steel

Mahira-Adna Cota Araujo, Jean-Bernard Vogt, Jeremie Bouquerel

Version of Record: https://www.sciencedirect.com/science/article/pii/S0142112321003042
Manuscript_03998b469586461a6ca08a0674182d85

Retained austenite-aided cyclic plasticity of the quenched 9Ni steel

Mahira A. Cota Araujo, Jean-Bernard Vogt*, Jérémie Bouquerel

Univ. Lille, CNRS, INRAE, Centrale Lille, UMR 8207 - UMET - Unité Matériaux et Transformations, F-59000 Lille, France

**corresponding author : jean-bernard.vogt@centralelille.fr*

Abstract

This study focuses on the low cycle fatigue mechanism of the quenched 9Ni martensitic steel containing retained austenite films at martensite laths. HRTEM and EBSD suggested that extrusions developed along Low Angle Boundaries or along High Angle Boundaries at low and high strain respectively. Short cracks grew along LAB at low strain while they used any kind of boundary as well as crossed the martensite laths at high strain. Retained austenite allowed a flowing of matter along interfaces by acting as a lubricant. Consequently, the Coffin-Manson relation exhibited a bilinearity with a change in curve slope at $\Delta\varepsilon_t = 1\%$.

Keywords: crack nucleation – martensite – cyclic softening – microstructures - extrusion/intrusions

1. Introduction

Due to the simple form of the Coffin-Manson relation, it is frequently employed by engineers to estimate the performance of a material in terms of resistance to crack initiation by low cycle fatigue (LCF). Indeed, the linear relation in a log-log diagram is very convenient to estimate the fatigue life as a material is subjected to a cyclic plastic strain range [1]. Though most of pure and engineering materials obey this relation and can be described with a simple equation,

some exceptions may exist where two equations in a range of plastic strain are needed. The reason for that is not related to data scattering but is connected with the microstructure which controls the crack initiation mechanism.

Different explanations linked to the bi-linearity of the Coffin-Manson relation are based on the way by which the mechanism of cyclic plasticity is accommodated. This is frequently observed in LCF of base nickel alloys, from room to high temperature. The change in slope is explained by the micro-twinning competing with dislocation slip in the nickel base alloy IN 718[2] or by the change in the number of operating slip systems [3]. Many different ferritic matrix alloys also exhibit the bi-linearity of the Coffin-Manson relation. In interstitial free steel [4], the formation of fine subgrains at high strain range was caused by dislocation–dislocation, and dislocation–precipitation interaction at low strain range. The accommodation of the deformation by ferritic islands in weak quantity in a 12Cr martensitic steel at low strain, and by both ferritic islands and the martensitic matrix was the reason for the observed bi-linearity. Recently, Marinelli et al showed out the bi-linearity of the Coffin Manson curve in a 16CrMnV7-7 bainitic steel and the role of the complex microstructure of this steel [5]. They pointed out the need to consider the different constituents (lath, block, and packet) of the bainitic grain in the crack initiation and propagation stages to interpret the presence of the double slope.

The present paper is concerned with a 9Ni martensitic steel, which LCF resistance curve could not be fitted with a single equation. As bainite, martensite exhibits a hierarchical structure. The finer martensitic structure is composed of light misoriented laths. During the martensitic transformation, the prior austenite grains are nucleation sites for the martensite variants (sub-blocks or laths) [6]. The groups of laths with the same variant disoriented by less than 10° are denominated as martensitic blocks. A martensitic packet is a group of parallel blocks that contains the laths with the same habit plane.

The 9Ni martensitic steel has also the particularity to contain an austenitic phase likely to form at interfaces, either retained austenite or reversed austenite, depending on the heat treatment [7–10]. This steel is widely used in the oil and gas sector due to the excellent cryogenic properties. It is normally commercialized in a tempered condition, with a certain amount of reversed austenite [11–13]. The conditions of the use of the components made of this material entail inevitably thermal cyclic stresses, which are one of the several types of LCF damage. To explain the presence of the two slopes in the Coffin Manson curve, it is necessary to understand the mechanism of cyclic plasticity and how it affects the initiation of short cracks. However, the number of studies on short crack initiation is more restricted when it comes to complex microstructure such as martensite found in steels. The crack embryo or intrusion is the very first stage of crack initiation and occurs at the surface. When dislocation glide is responsible for cyclic deformation accommodation, the formation of intrusion is soundly explained by Polak and Man's concepts especially for monocrystals or rather simple microstructure engineering materials such as austenitic stainless steels [14]. This implies first the formation of an extrusion resulting from active localized plasticity in persistent slip band (PSB) e.g., and then matter displacements and vacancies accumulation at the interface between the PSB and the other dislocation structure phase such as the matrix (vein-channel dislocation phase). Tough these dislocation structures were not encountered in a fatigued 12Cr martensitic steel, the Polak and Man's concept could be applied to this material by considering the lath interface as the PSB/ matrix interface [15]. It is therefore questionable if a very small interface modification, such as the presence of a secondary phase, can play a role in the nucleation of the persistent slip marks and of intrusions.

The objective of the paper is to investigate the LCF behavior of a 9Ni steel in the quenched condition. The mechanical response, stress response to strain cycling as well fatigue resistance will be presented. Then a deep analysis of the microstructure will be carried out to explain the

specific observed behavior. This will rely on the analysis of the microstructure after fatigue by considering the different scales from the laths to the prior austenitic grain boundaries. Attention will be paid to the role of the retained austenite present along the martensite laths. Especially, it will be examined if any TRIP effect governs or not the fatigue behavior of the considered 9Ni steel.

2. Material and Experimental Procedures

The investigated material is a low carbon martensitic steel for which the main elements of the chemical composition in weight % were provided by the supplier: 0.04 C, 8.99Ni, 0.53 Mn, 0.23 Si. The sample was austenitized at 900 °C followed by water-cooling.

To get a general idea of the microstructure, the bulk sample was mechanically polished and finished with 1 µm diamond paste, chemically etched with Nital 3% solution, and analyzed by Light Optical Microscopy (LOM) and Scanning Electron Microscopy (SEM). Additionally, Vickers hardness measurements were performed.

An estimation of the phases present in the steel prior and after fatigue was performed by X-ray diffraction (XRD) with a Rigaku Smartlab Diffractometer in a 38-120° 2Θ range by using Cu-kα radiation (λ = 1.54056 Å). The Cullity method [16] was used to calculate the austenite content.

Transmission electron microscopy (TEM) allowed the examination of the dislocation structure in the initial state. Thin foils were cut from the rolling direction, mechanically ground, and thinned up to 80 µm. The 3 mm thin disks were subsequently thinned by Struers Tenupol double jet polisher using a solution of 90% acetic acid and 10% perchloric acid at 12 °C and 20.5 V of applied tension. Finally, the disks were afterward cleaned using Precision Ion Beam Polishing (PIPS). The thin foils were analyzed by FEI Tecnai Transmission electron microscope G2-20 twin operated at 200 kV.

Flat LCF specimens were cut according to ASTM E606 by spark erosion. The specimens with a gauge length of 12 mm and a cross-section of 6 mm x 3 mm were prepared by mechanical polishing and finished with a ¼ µm diamond paste. Additionally, a fine-polishing step with Struers OP-U 0.04 µm colloidal silica suspension was done to obtain a proper smooth surface for post-deformation analysis. Interrupted LCF tests and tests up to failure were undertaken at room temperature at several constant strain ranges ($\Delta\varepsilon_t$ = 0.8%, 0.9%, 1%, 1.2%, and 1.6%) using a reversal triangular waveform with a constant strain rate of $4x10^{-3}$ s^{-1} and a strain ratio R_ε = -1.

The bulk specimen and its surface prior and after cyclic straining were investigated by Electron Backscatter Diffraction (EBSD-SEM) in a Hitachi SU-5000 FEG-SEM system operated at 20 kV with an Oxford Instruments® EBSD system having a minimum angular resolution of 0.5°. The post-processing of the data was perfomed using the EDAX/TSL OIM 7.3 software. For each considered conditions, two EBSD acquisitions of at least an approximate area of 60 µm x 40 µm in order to cover about 100 blocks and 47 packets The scan step size of 100 nm was adopted focusing on optimization of the acquisition data according to the methods proposed by Chen et al. and Kamaya et al. [17–19], where a small step size can collect background data inducing errors, and higher values lead to loss of information. Grain dilation with a tolerance angle of 15° was applied to clean up the artifacts present on the material surface [5]. To achieve a better understanding of the relationship between crystallography character and the susceptibility to fracture, Martensite Parent Grain Reconstruction based on the 24 Kurdjumov-Sachs variant orientation relationship was accomplished by an algorithm developed for MTEX analysis toolbox in MATLAB [21].

To observe the dislocation structures in a wider area, EBSD-based controlled Electron Channeling Contrast Image (c-ECCI) was carried out in the same microscope. The two-beam diffraction condition for a well-oriented crystal was obtained with the aid of the TOCA

software using the c-ECCI methodology developed by Zaefferer and Elhami [20]. Microstructural evolution at different life fractions was accomplished by the SEM-EBSD technique.

To complete the analysis, cross-sectional lamellas were extracted by the Focused-ion beam technique (FIB). Selected zones with pairs of extrusions-intrusions were chosen based on the EBSD scans. High-resolution transmission electron microscopy (HRTEM) in a FEI TITAN Themis 300 microscope allowed the observations of the deformed sample structure and the PSM's location.

3. Results and Discussion

3.1 Microstructure characterization before deformation

The 9Ni steel with the adopted processing route exhibits a martensitic structure as shown in Figure 1a.

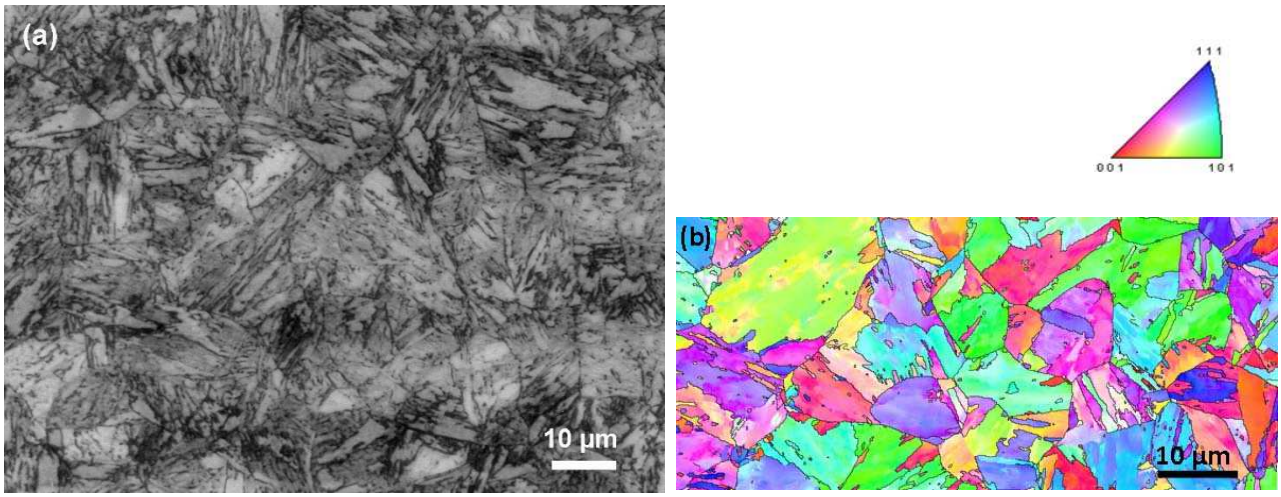

Figure 1 – Light optical micrograph (a) and IPF image (b) of the 9Ni steel austenitized at 900°C and water quenched

By using the mean linear intercept method of ASTM E112 standard, the martensitic microstructure was characterized with an average grain size is 14 µm (standard deviation of

6.55 µm), a packet size of 5 µm, and a block size of 3 µm. The material presented a Vickers Hardness of 362 HV10.

At this scale, the substructure in terms of blocks and packets inside the primary austenitic grain boundaries is evidenced. Moreover, the EBSD IPF map shows that the material does not have a preferential texture (Figure 1b). However, for the considered acquisition parameters, the expected austenitic phase was not revealed by this technique even though some individual pixels were assigned as the austenite. Yet, the volume fraction has been estimated in an amount of 8% from the XRD diffractogram and by using the Cullity relation.

TEM in the imaging mode and in the Selected Area Diffraction (SAED) mode was successful to unambiguously image the retained austenite. This has been found in the form of very thin films, as reported in the literature [22,23] but in sufficient amount to provide enough intense diffraction spot. By selecting the right diffraction spot (Figure 2b), the dark-field images highlighted the austenite along the lath boundaries (Figure 2a).

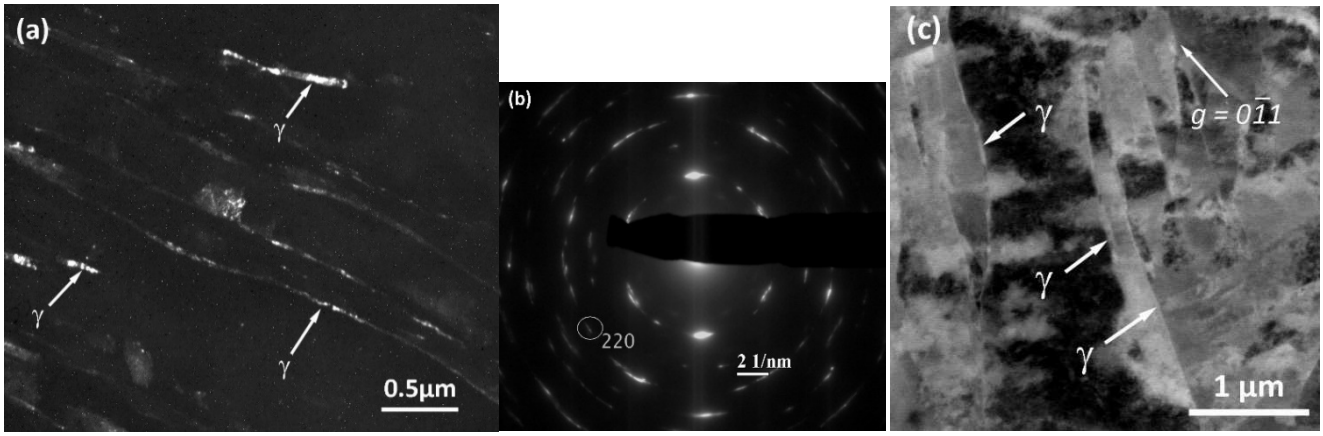

Figure 2 – a) Dark field image obtained by the selected 220 spot of FCC austenite, b) Selected area electron diffraction (SAED) pattern obtained from the same bright field image in 2a. c) c-ECCI image showing a lath interface with a probable austenite film highlighted by the arrows.

By analogy, considering the different contrast and morphology at the boundaries, it is reasonable to assign the narrow trims between the martensite laths as austenitic films as the arrows point in the corresponding c-ECCI image of Figure 2c. TEM and c-ECCI showed that the martensite laths have a width of several hundreds of nanometers fulfilled by a high density of dislocations (Figure 3).

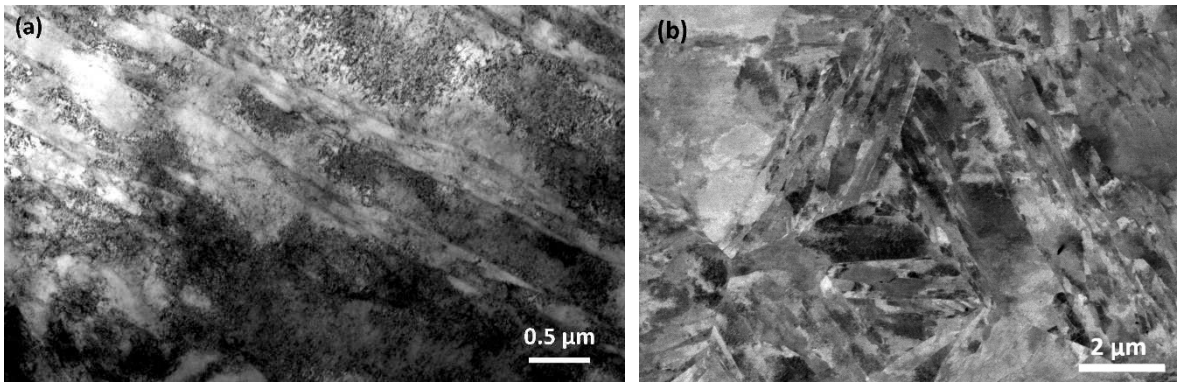

Figure 3 – TEM bright-field image (a) and c-ECCI micrograph (b) of the microstructure before fatigue

At a more mesoscopic scale, the EBSD-LSM (Line Segment Method) presents the spatial distribution of the boundary traces associated with a specific misorientation. High Angle Boundaries (HAB) corresponds to 15° misorientation between the measured points; usually, they are equivalent to the grain boundaries highlighted by LOM. Although this is not the case of the martensite, where those misorientations can also correspond to packets or sometimes blocks, a parent grain reconstruction is necessary to differentiate the martensitic structure based on the variant orientation; this topic will be further discussed. In LSM maps, the Low Angle Boundaries (LAB) comprised between 1-15° can be correlated to laths, subgrains, or dislocations structures. The LAB were subdivided into groups of misorientations between 1-5°, corresponding to dislocation tangles, and misorientations between 5-15° were classified as microstructural substructures such as subgrains or dislocation cells.

Figure 4 superposes the image quality map (IQ map) and the LSM map of the 9Ni steel prior to

deformation. It already shows that such an initial complex structure exhibits intrinsic substructures. Such arrangements can be assigned to laths and blocks interfaces and even dislocations cells if they have formed.

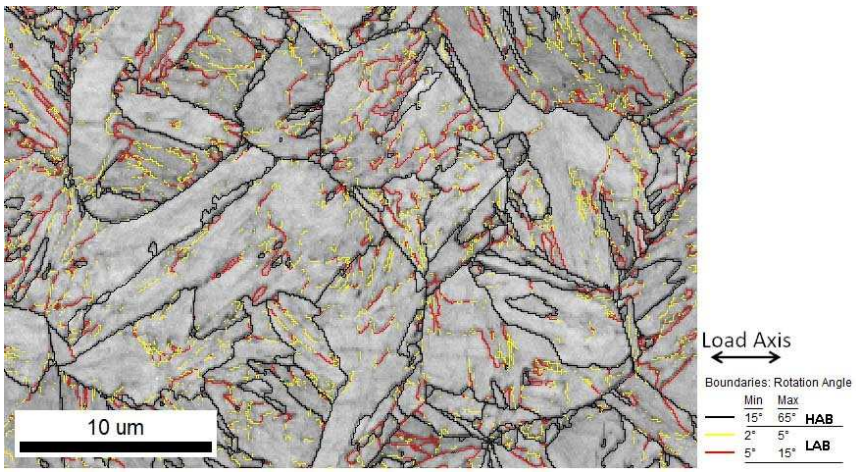

Figure 4 – Image Quality + LSM EBSD maps for the water quenched 9Ni steel at the initial state. High Angle Boundaries (HAB): black lines; Low Angles Boundaries (LAB) yellow and red lines

3.2 Cyclic stress-strain response and fatigue resistance

The curves of cyclic accommodation for the tests performed at the different total strain ranges are displayed in Figure 5. The graphs represent the evolution of the stress amplitude versus the number of cycles (Fig. 5a) as well as a function of the fraction of fatigue life (Fig. 5b).

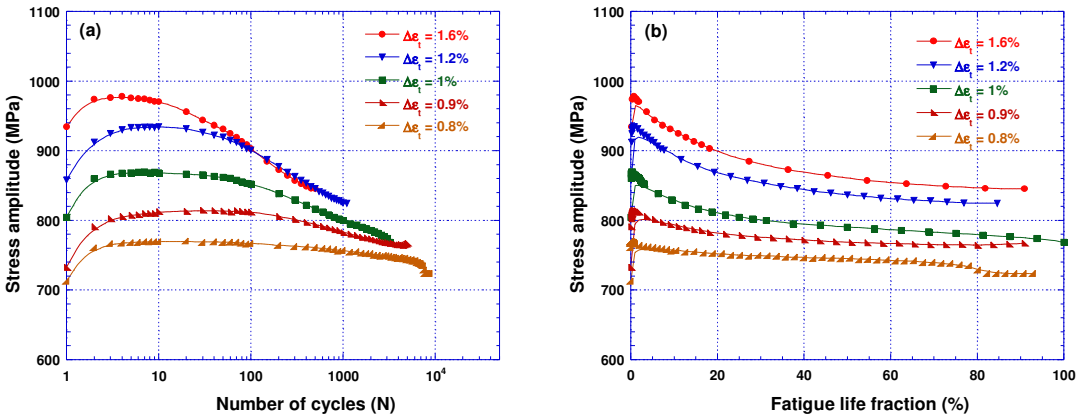

Figure 5 – Evolution of the stress amplitude versus (a) the number of cycles and (b) the fatigue life fraction for the different total strain tests

All curves indicate that the response of the material consists of an initial cyclic hardening followed by a cyclic softening and then nearly quasi stabilization of the stress. The hardening period is shorter as the total applied strain increases and represents a very small part of the fatigue life (less than 2 %). By contrast, the softening period is more pronounced when the applied deformation is greater.

The cyclic stress-strain curve obtained from the quasi stabilized hysteresis loop is shown in Figure 6, together with the curve obtained from the peak stress of cyclic accommodation and the monotonic hardening curve. In the stabilized part of the cycling, the stress softening is more pronounced at higher strain levels. It can be seen that the initial hardening is very moderate in comparison with the cyclic softening. This suggests that the application of external stress allowed releasing the numerous entangled dislocations in the martensite laths as soon as the material is under cycling. High strain loading results in high stress and in a higher amount of unlocked dislocations, which can glide and recover the laths leading to pronounced softening. A dislocation rearrangement leading to a more stable configuration is also expected, which needs to be shown.

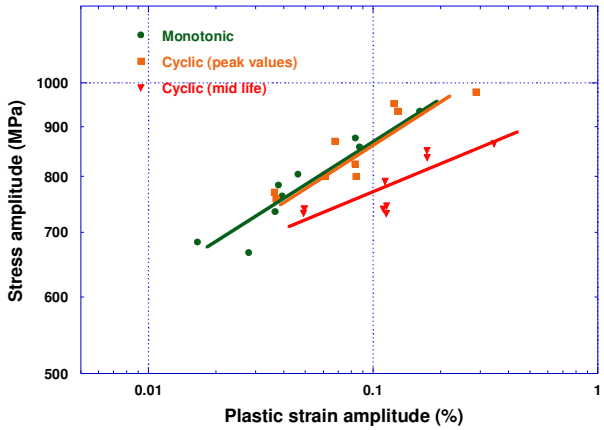

Figure 6 – Cyclic and monotonic stress-strain curves

The plot of the different components of the strain range versus the number of cycles to failure is shown in Figure 7. The plastic strain range was measured on the loop recorded at mid-life

by the wideness of the loop at zero stress. The elastic strain range was measured by the difference between the total strain range and the plastic strain range.

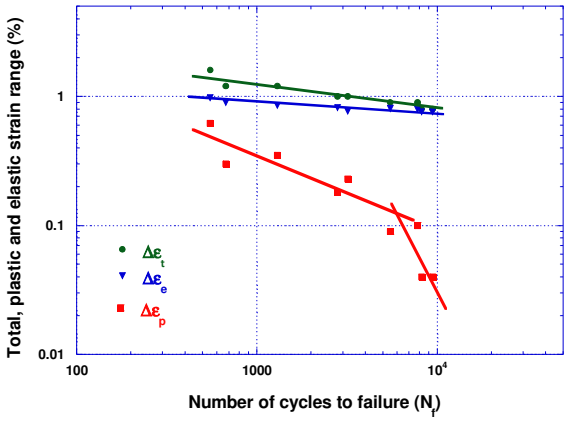

Figure 7 – Manson-Coffin diagram showing a change in slope at $\Delta\varepsilon_p$ =0.2% ($\Delta\varepsilon_t$ =1%)

Under all of the experimental strain ranges, the elastic strain range was nearly constant and the associated line (the Basquin curve) stays above the plastic strain range data. This is encountered for some martensitic steels [24]. However, fitting the plastic strain range data according to the number of cycles to failure with a single line (the Manson-Coffin curve) was not possible. Indeed, a bilinear behavior of the quenched microstructure with a transition state at $\Delta\varepsilon_p$ =0.2% ($\Delta\varepsilon_t$ =1%) is observed.

To provide an explanation of this change in slope of the fatigue resistance curve, it was decided to investigate the microstructure after fatigue at low and high strain tests ($\Delta\varepsilon_t$ = 0.9% and 1.2%). The evolution of the microstructure and of the damage was also considered at three stages of cycling: at the peak stress in the cyclic accommodation curve (σ_{max}), 5%, and 50% of the fatigue life

3.3 Metallurgical investigation of the relief developed during low cycle fatigue tests

3.3.1 $\Delta\varepsilon_t = 0.9\%$

Figure 8 shows the evolution of the same zone of the external surface analyzed by c-ECCI for several stages of the fatigue life. This zone was not imaged before cycling because it could not be predicted if it would have been activated later on.

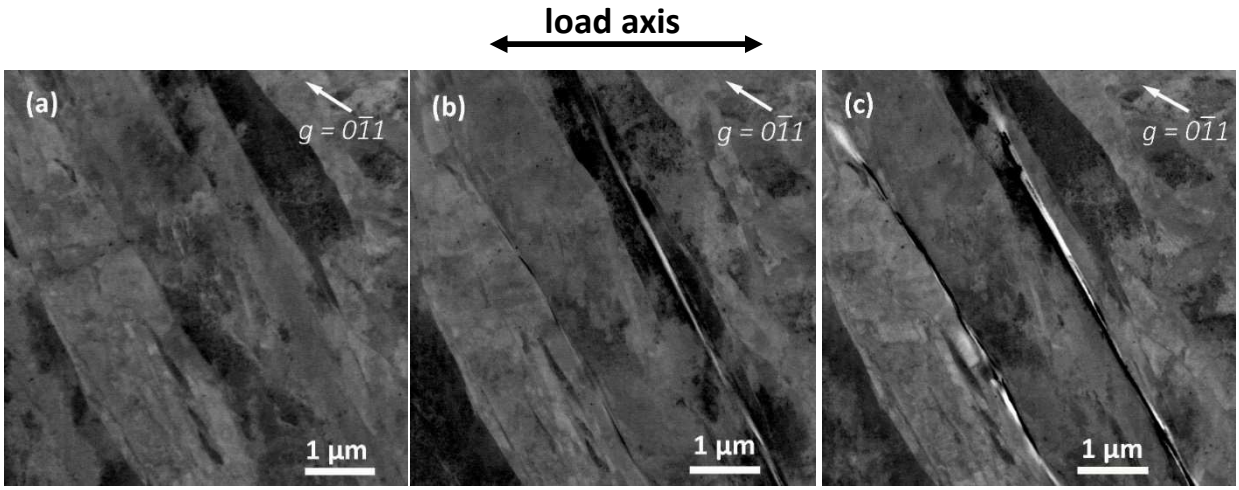

Figure 8 – c-ECCI images showing the dislocations and the topography of the water quenched 9Ni steel at (a) the cyclic hardening peak, (b) 5% and (c) 50 % of the fatigue life ($\Delta\varepsilon_t = 0.9\%$)

For the test performed at $\Delta\varepsilon_t = 0.9\%$, at σ_{max} ($\Delta\varepsilon_p = 0.16$), the slip steps are already present but not abundant and not easily seen either, as can be observed in Figure 8a. A small surface relief was identified in few zones but they were sometimes related to the martensitic structure, not the slip steps. The slip steps confirmed the ability of the quenched steel to accommodate the plastic deformation and they are the first evidence of the rising of an incipient extrusion. The latter is indeed easily developed as can be seen in Figure 8b after 5 % of the fatigue life ($\Delta\varepsilon_p$ = 0.19). With the increased number of cycles, the former extrusions grew and new ones formed. As well, intrusions in the vicinity of the extrusion are visible (Figure 8c). Extrusion and

intrusion both presented difficulty to determine their exact location, interface (lath boundary, block boundary…) or inside a martensite lath.

Figure 9 gives a closer observation at the vicinity of an extrusion at 50% of fatigue life ($\Delta\varepsilon_p$ = 0.22) by means of the c-ECCI technique. By considering the evolution of the microstructure at different fatigue lives, it was globally observed that the dislocations had a tendency to be swept and to concentrate towards the deformed zones (extrusions-intrusions), creating new very small cells and subgrains, cleaning the interior of these structures. Moreover, a very thin fragmented wall dislocation arrangement was also evidenced

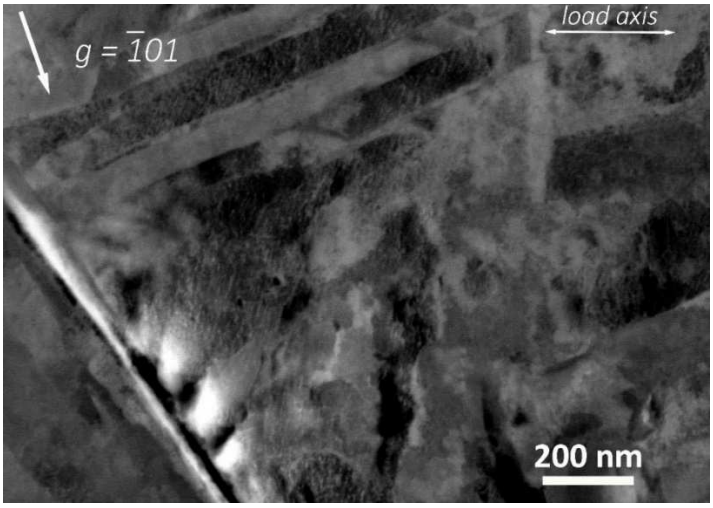

Figure 9 – Planar dislocation structure localized within the laths next to the persistent slip marks at 50% of the fatigue life for the test at $\Delta\varepsilon_t$= 0.9%

Since the slip activity appears concentrated near the extrusion, LSM maps were considered to check if dislocation arrangements and restructuration near the extrusions have occurred (Figure 10). But as well, no difference was visible between the various regions scanned after the fraction lives. Some zones pointed by blue arrows show changing of disorientation levels, passing from 1-5° to 5-15°, and some evolving to 15° of misorientation, all comprised inside a probable prior grain.

Since metallurgical interfaces such as grain boundaries or twin boundaries can result in strain incompatibility, they are a potential site for crack initiation. But, this question arises more intensively since martensitic steel contains a lot of different interfaces The description of the martensitic structure only with the elements of the hierarchical feature is not sufficient and must include the determination of the orientation relation of blocks and laths with the parent austenite. According to recent studies in dual-phase ferritic-martensitic steels, the prior austenite grains boundaries were identified as crack nucleation sites [25]. On the other hand, it has been also reported that the martensite properties are presumably linked to the block size and their misorientation [26].

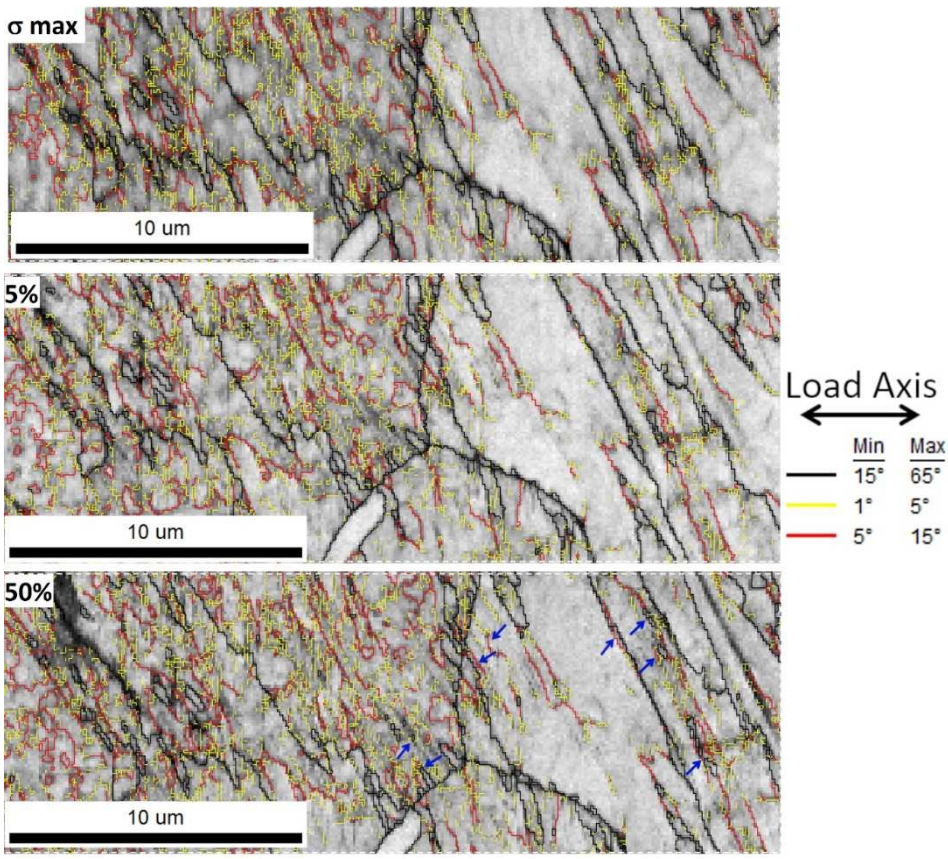

Figure 10 – EBSD grain boundary maps and misorientation partition for the 9Ni steel at $\Delta\varepsilon_t$ = 0.9%. The darker zones indicate the regions with the presence of extrusions. Blue arrows indicate the changing of misorientation level.

The major drawback regarding the preliminary EBSD results is that IPF maps nor LSM maps can make a good distinction of the different martensitic units, especially in the case of austenite parent grain. To resolve this issue, a parent austenitic grain reconstruction turns out to be essential, differentiating the several martensitic features such as packets, blocks, and grain boundaries, allowing the correlation with mechanical properties and fatigue response. As the orientations relationships (OR) such as Greninger-Troiano, Nishiyama- Wassermann, and Kurdjumov-Sachs are approximations and differ from each other by a small degree [27], the 24 Kurdjumov-Sachs variant orientation relationship was adopted for the martensite parent grain reconstruction in this study. The martensitic transformation involves a restricted set of 24 possible Kurdjumov-Sachs variants, in which the same closed packet plane in austenite is parallel to the transformed martensitic closed packet plane: $\{111\}\gamma//\{110\}\alpha$, as well as the directions: $[110]\gamma //[111]\alpha$, where a small deviation from 1.5 to 3° is inherent to metallurgical inhomogeneities related to the martensitic transformation. In this experiment, the average angular deviation-error obtained from the reconstruction ranged between 2° to 4°, showing as an acceptable fit. The grain reconstruction allowed the differentiation of the variants, denominated as sub-blocks or laths, by means of different shades. A packet contains a small gradient of a specific color comprising a set of three parallel blocks, each of them with a very slight color change. The gradient bar present in Figure 11 will clarify this concept. Figure 11exhibits the martensite parent grain reconstruction based on the Kurdjumov-Sachs orientation relationship for the deformed zone, the parent grain is delimited by the dark line, an equivalent IPF map was also added to contrast the results. The two scanned zones by EBSD containing extrusions were reconstructed to get a general idea of the behavior of the material. It was observed that the extrusion development is restricted exclusively to the structures which have nearly the same orientation (lath/lath and lath/block) belonging to the martensitic grain, those less disoriented structures are indicated as a singular color in the reconstructed image,

representing the laths and blocks. With the support of the c-ECCI findings, the conclusion is that the dislocations are limited to move only across the LAB corresponding to block and laths interfaces. In this case, the strain is accommodated within such martensite units.

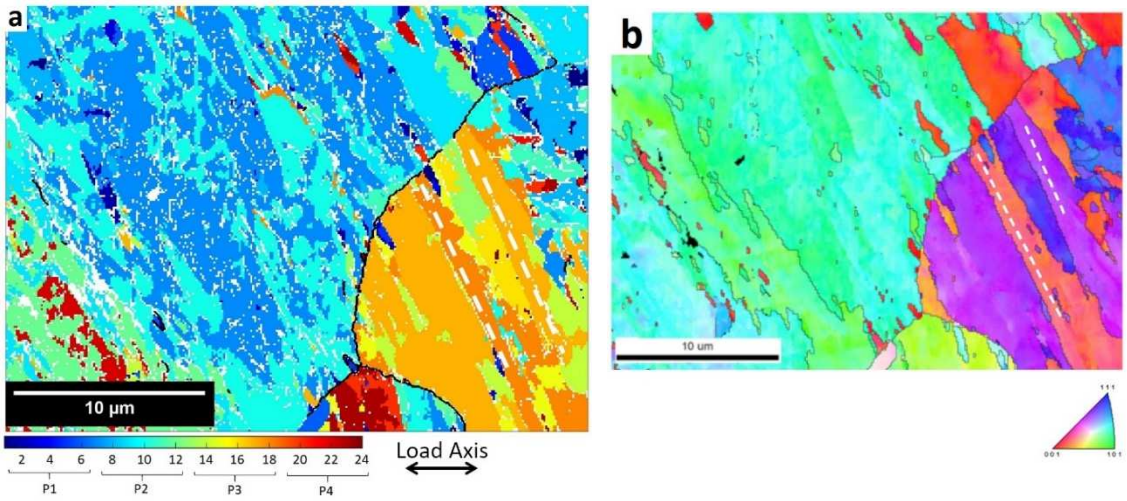

Figure 11 – (a) Martensite parent grain reconstruction based on the Kurdjumov-Sachs orientation relation for the 9Ni steel deformed at $\Delta\varepsilon_t$ 0.9%. (b) Corresponding IPF map. The white dashed lines indicate the extrusions.

3.3.2 $\Delta\varepsilon_t$= 1.2%

For the test performed at $\Delta\varepsilon_t$ = 1.2% and after the number of cycles where the peak stress value was obtained (σ_{max} stage-$\Delta\varepsilon_p$ = 0.31), few extrusions have already developed at the surface (Figure 12a). With further cycling, the first formed extrusions grew and additional new other ones emerged (Figures 12b and 12b). During the softening stage ($\Delta\varepsilon_p$ = 0.36), arrays of dislocations were found next to extrusion at the selected crystallographic plane, cell configuration was also observed (Figure 13). These arrays of dislocations could be very thin highly dense dislocation walls (HDDW) as already identified in TWIP steels, CrMn steels, Fe3Si, and austenitic stainless steels. The HDDWs can impede the dislocation glide [28–35].

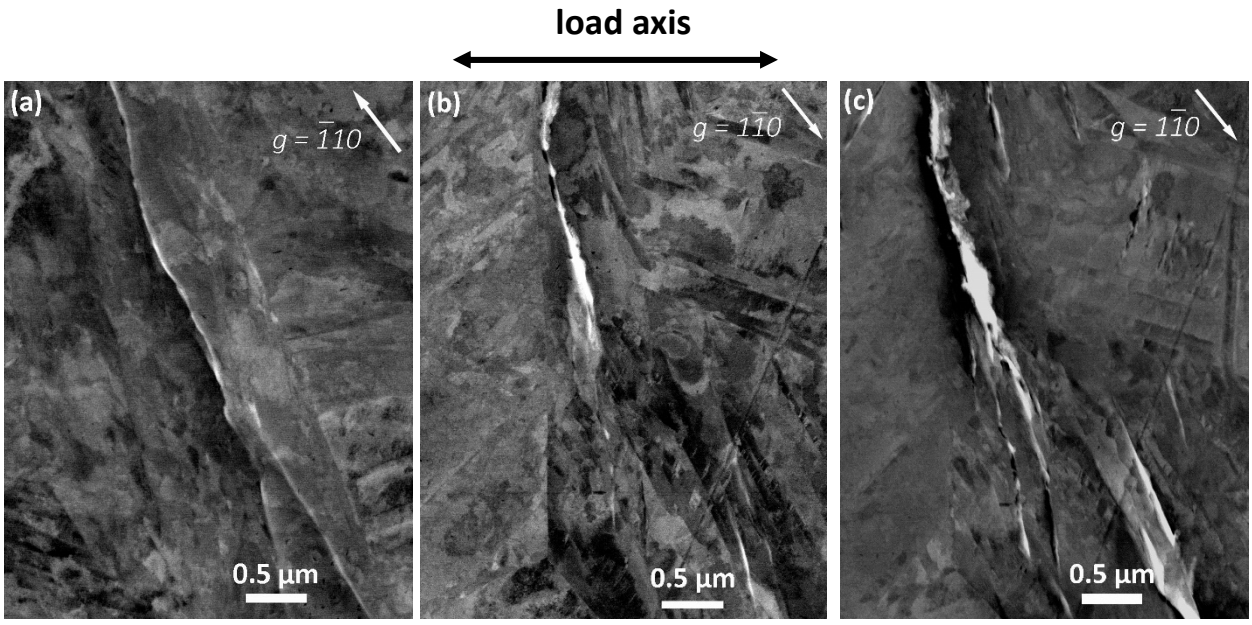

Figure 12 – c-ECCI images showing the dislocations and the topography of the water quenched 9Ni steel at (a) the cyclic hardening peak, (b) 5% and (c) 50 % of the fatigue life ($\Delta\varepsilon_t$ = 1.2%)

HDDW is a terminology adopted for fine linear structures originated from coplanar slip oriented in most favorable slip directions. It was also observed in our material that the zones previously fulfilled by dislocations were replaced by more organized structures such as cells and subgrains, those dislocations arrangement restricts the mean dislocation free path.

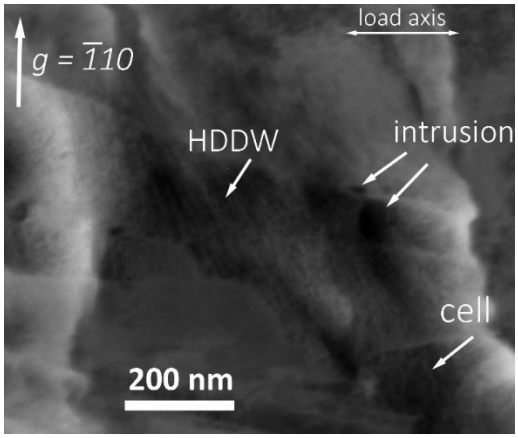

Figure 13 - Highly dense dislocation walls (HDDW) aligned to a persistent slip mark which crosses a block boundary. One intrusion in the process of forming at the interface ($\Delta\varepsilon_t$ = 1.2%).

LSM maps (Figure 14) indicate that strain is mostly related to the evolution of the LAB. It was remarked an increase in 1°-type LAB, as well as their evolution into 5° of misorientation, while no change in terms of HAB was observed. Some preexisting HAB were however sites for extrusion development.

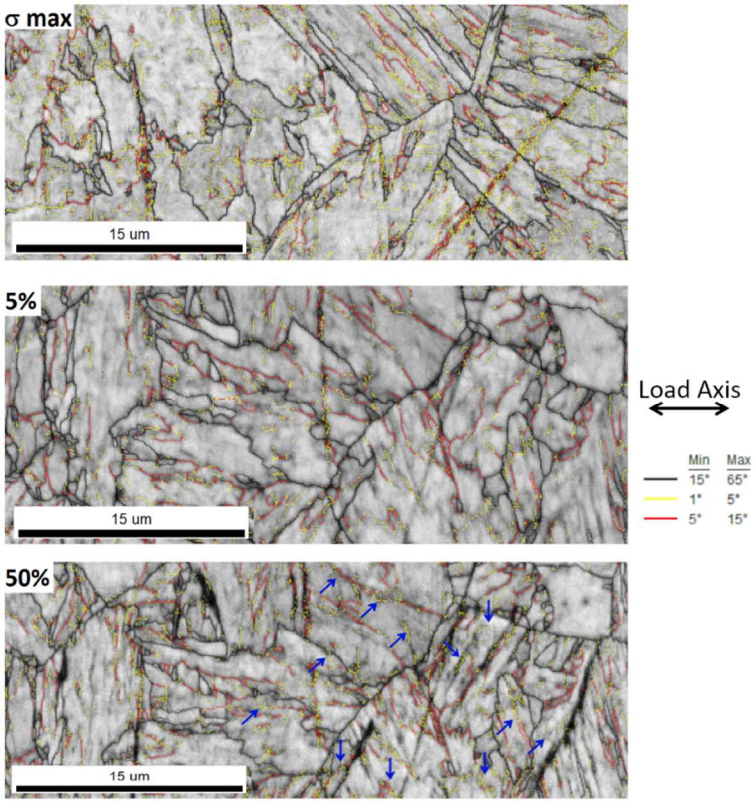

Figure 14 – Image Quality + LSM EBSD maps for the 9Ni steel at $\Delta\varepsilon_t$ = 1.2%. The darker zones indicate the regions with the presence of extrusions. Blue arrows point to the new LAB.

Martensite parent grain reconstruction based on the Kurdjumov-Sachs orientation relationship (Figure15) indicates that, differently from the lower level of applied deformation, the extrusions develop more frequently at HAB, crossing all types of LAB and low angle misoriented structures. The main extrusions are present in HAB (comprising packets and PAGB). As the cycling continues, the extrusions may coalesce or even propagate trespassing all kinds of interfaces present in the material. Those findings indicate that at high levels of deformation, the boundaries could not hinder the development of the extrusions anymore.

Those observations of the crack formation and their relation to the level of disorientation in microstructure were also noticed in macro tensile tests of lath martensite [36]. At small strains, the deformation due to crystallographic slip parallel to lath boundaries prevails, although, at high strains, the deformation is governed by crystallographic slip at HAB. A certain amount of energy must be provided to trigger the movement of dislocations in a long-distance range. At very small strains, the slip activity tends to concentrate within the laths, however, at higher strains, the dislocations are able to surpass the LAB but then they tend to pile up at the HAB, raising the stress levels at those zones.

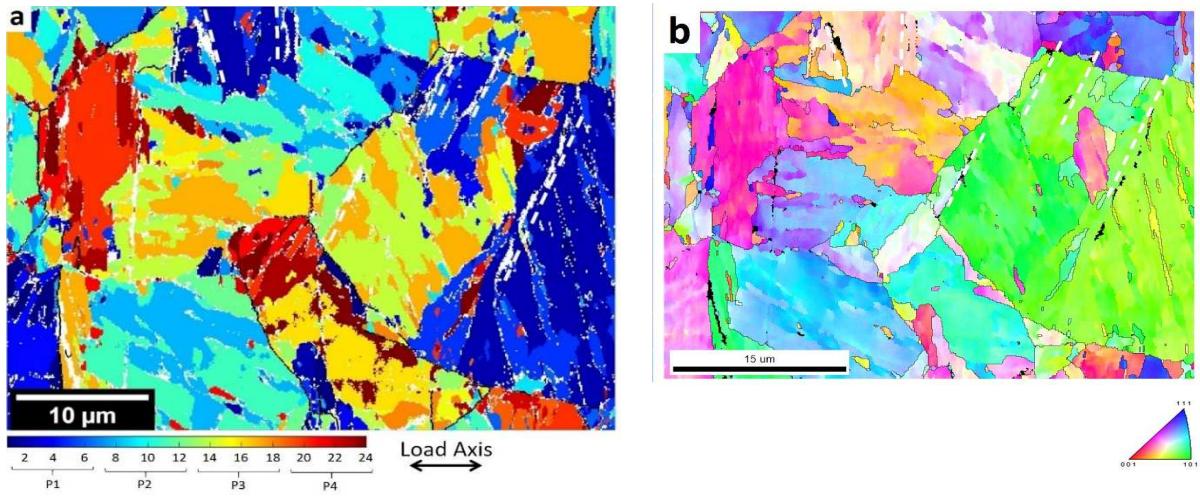

Figure 15 – (a) Martensite parent grain reconstruction based on the Kurdjumov-Sachs orientation relation for the 9Ni steel deformed at $\Delta\varepsilon_t$ = 1.2%. (b) Corresponding IPF map. The white dashed lines indicate the extrusions.

3.4 Accurate determination of extrusion/intrusion location

A typical SEM image of the surface relief formed by fatigue is displayed in Figure 16 for a test performed up to failure at $\Delta\varepsilon_t$ = 1.2%. The picture has been taken far from the main crack. Isolated extrusions with significant extruded mass are clearly identified and coalescence of

intrusions (microcracks) is also noticed. A similar pattern of extrusions/intrusions was also observed for low strain tests except that the extrusions were much less numerous and much less developed. The precise determination of the extrusion and intrusion in regards to the microstructure is very difficult from direct observation of the specimen surface. Besides the question of resolution, the extrusion has its own thickness and shape. As pointed out by Polak [37], even by using atomic force microscopy (AFM), the inclination of the extrusion or its curved aspect can screen the material below.

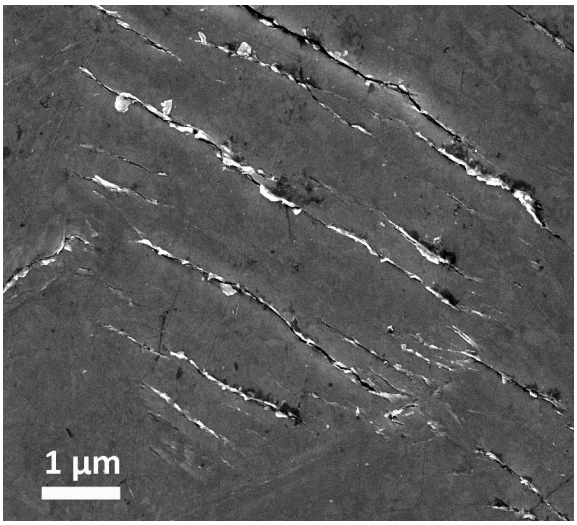

Figure 16 – SEM image of typical persistent slip marks found at the end of fatigue life ($\Delta\varepsilon_t = 1.2\%$)

To have a real view of the shape of the extrusion and its exact location, TEM observation was performed on FIB lamellae extracted from identified extrusions. Cross-sectional cuts were performed on the specimen surface, the lamellae were parallel to the load axis. The sample fatigued at $\Delta\varepsilon_t = 1.2\%$ was chosen for this investigation because it presented more prominent and numerous sets of PSMs at several stages of fatigue life.

At 5% of life, single extrusions were already voluminous and evident (Figure 17a). The surface was composed predominantly of extrusions, no developed intrusion was found beside a timid formation next to extrusion. It can be seen that the extrusion is located at the border of a lath

interface while the intrusion is in the middle of the lath. Finally, on the sample taken at the end of life, short cracks stemming from the intrusion were identified and a transition in the behavior from an intrusion to a short crack is evident (Figure 17b). The central intrusion present in Figure 17b starts in the middle of the lath changing its path towards the HAB boundary, where it will finally meet the requirements to grow and propagate.

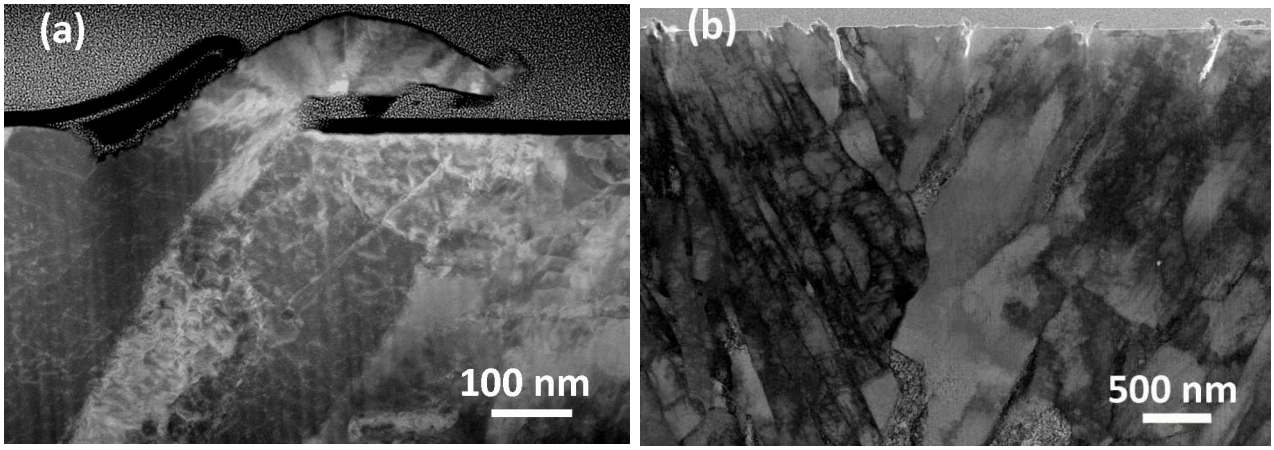

Figure 17 – HRTEM images of thin lamellas showing accurately the sites of extrusions and intrusions at (a) 5% and (b) 50% of the fatigue life of the test performed at $\Delta\varepsilon_t$= 1.2%

Those visualizations corroborate with the statement done by Pólak and Man [14] that the pair of extrusions-intrusions are the precursors of a crack. But the main difference between the present observation with those on copper, austenitic stainless steels, or even with 12Cr martensitic steel is that the intrusion is not located exactly at the interface.

The TEM images did not show any specific dislocation structure such as PSB that would express cyclic strain localization inside a martensitic lath. Nevertheless, the volume of the extrusion suggests a high activity of plastic deformation, which is confirmed by the very small dislocation cells inside the lath. Note that the retained austenite could not be seen as a detrimental effect of the FIB lamellae preparation which tends to transform it due to the high amount of energy applied during the machining. It turns out that the lath/lath interface plays a major role in the cyclic accommodation of the deformation.

3.5 Mechanism of cyclic plasticity and of cracking of the quenched 9Ni steel

As mentioned in the introduction, the bilinear Coffin-Manson behavior is finally observed in a lot of situations. The origin is however different and depends on the microstructure of the material which governs the homogeneity of plastic deformation partition and the process of short crack initiation. The retained austenite sandwiched between martensite laths is suspected to take part in the accommodation of the cyclic plasticity but not as this occurs in TRIP steels where the austenite transforms into α' martensite. XRD analysis performed after the LCF test in this study indicated a small decrease in the austenite content, from 8% to 5%, meaning that the retained austenite is quite stable upon cycling. Therefore no TRIP effect has to be considered here. The role of the retained austenite in the present quenched 9Ni is likely to allow the matter to flow along the interface and to act as an interlath lubricant for boundary sliding. Such a mechanism of boundary sliding has been suggested by Du *et al* on water quenched martensite deformed by micro tensile test who indicated a prevalent boundary sliding mechanism unlike crystallographic slip [38].

For the quenched 9Ni steel considered in this study, the bilinear Coffin-Manson is related to the interactions of moving dislocations and their interactions with LAB interfaces, the latter being coated by the lubricant retained austenite.

At lower strains, the entangled dislocations produced during the quench become released and move inside the martensite laths with difficulty and for a short distance. As a result, they meet the first LAB (lath/lath and lath/block) which acting as a structural barrier do not allow the overcoming. Instead of establishing a pile-up of dislocations that would have generated increasing stress at the interface, a localized displacement of matter along the martensitic lath is possible thanks to the presence of retained austenite which acts as a lubricant. A highly localized plastic slip occurs in the zone giving rise to an extrusion along the LAB interface, and then the nucleation of the intrusion inside the lath.

However, at high strain levels, the moving dislocations in the martensite laths also encounter the LAB interface but being under higher stress can overcome this barrier. They do not stop and the matter displacement along the LAB interface does not occur. Instead, these dislocations pass over these LAB barriers until they reach the HAB interface. Now, as for low strain loading, the matter will flow along the interface aided by the presence of the lubricant film of austenite. An extrusion forms along the HAB boundary while an intrusion nucleates later on inside a martensite lath next to this HAG interface.

Though crack embryos do not nucleate along a LAB or HAB interface but inside a lath, their evolution into short crack occurs the nature of interface where the extrusion formed previously. In that sense, our results go in the same direction as those reported by Zhang et al [39] and Marinelli et al [5] who correlated the microstructure stability and boundaries compatibility to the crack initiation mode.

Figure 18 summarizes the process of extrusions/intrusions nucleation and growth during the fatigue life of the quenched 9Ni steel loading according to the strain level.

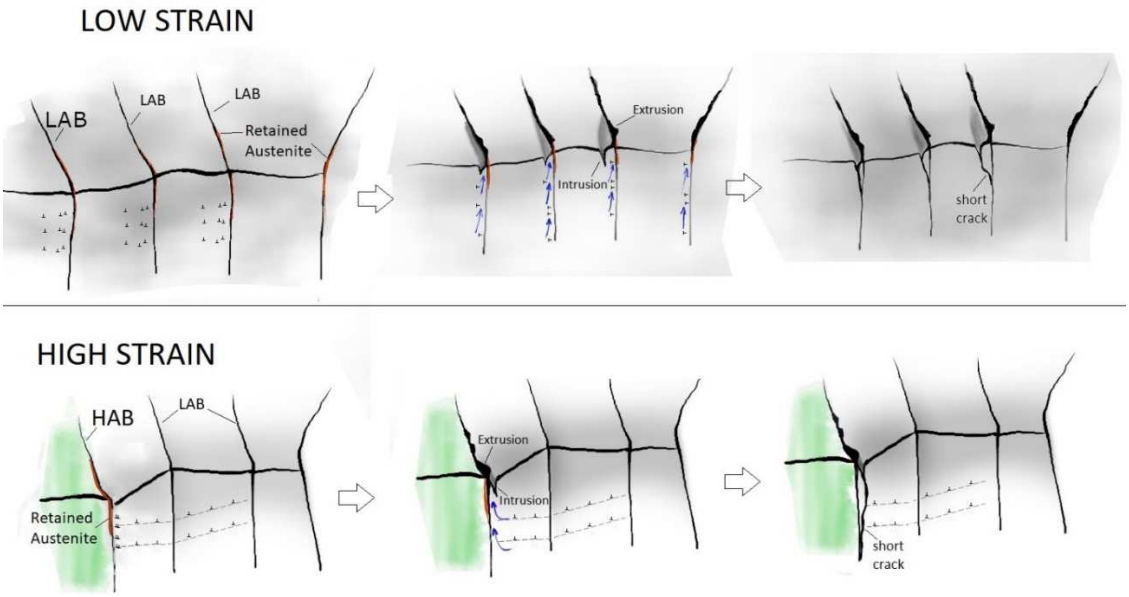

Figure 18 – Representation of extrusions and intrusions nucleation sites for the quenched 9Ni steel during fatigue at low and high strain

4. Conclusion

The low cycle fatigue behavior of a quenched 9Ni steel has been investigated with special attention on the mechanism of cyclic plasticity and crack initiation.

The mains results are as follows:

- The microstructure of the material comprises a martensitic matrix with nanofilms of retained austenite in a volumic fraction of 8%
- The cyclic accommodation consists of a short primary hardening followed by softening
- The Manson-Coffin relation exhibits a bilinearity and the change in the curve slope is at $\Delta\varepsilon_t$ = 1%
- HRTM images proved that extrusions develop along interfaces; intrusion nucleates beside in the middle of the lath and then deviates towards the high angle boundaries (HAB)
- Nanofilms of austenite allows the flowing of matter along interfaces by a lubrication effect
- At low strain ranges, low angle boundaries LAB (laths and blocks) act as a microstructural barrier to dislocation displacement and extrusion forms at their interfaces by a boundary sliding mechanism aided by interfacial austenitic films
- At high strain ranges LAB barriers can be overcome by moving dislocations which however meet another type of barrier, the high angle boundaries HAB (packets and prior grain boundaries) along which plasticity occurs also by a boundary sliding mechanism aided by interfacial austenitic films
- Short cracks grow along LAB at low strain while they use any kind of boundary as well as cross the martensite lath at high strain

Acknowledgments

The SEM and TEM national facility in Lille (France) is supported by the Conseil Regional des Hauts-de-France and the European Regional Development Fund (ERDF).

The authors thank technical engineer J. Golek for his help in the fatigue experiments.

One of the authors (M.A.C.A) would like to acknowledge the partial financial support of the Roberto Rocca Education Program.

References

[1] Cooper, C V; Fine ME. Coffin-Manson relation for fatigue crack initiation. J Vol 56; Conf TMS-AIME Fall Meet Detroit, MI (USA), 16-20 Sep 1984; J ID ISSN 0197-1689 1984;18:4–7.

[2] Bhattacharyya A, Sastry GVS, Kutumbarao V V. On the dual slope Coffin-Manson relationship during low cycle fatigue of Ni-base alloy in 718. Scr Mater 1997;36:411–5. https://doi.org/10.1016/S1359-6462(96)00405-8

[3] Ye D, Ping D, Wang Z, Xu H, Mei X, Xu C, et al. Low cycle fatigue behavior of nickel-based superalloy GH4145/SQ at elevated temperature. Mater Sci Eng A 2004;373:54–64. https://doi.org/10.1016/j.msea.2004.01.045

[4] Majumdar S, Bhattacharjee D, Ray KK, Ray RK. Bilinear coffin-manson relationship in thin sheets of interstitial-free steel. Metall Mater Trans A Phys Metall Mater Sci 2013;44:1714–21. https://doi.org/10.1007/s11661-012-1514-9

[5] Marinelli MC, M.Balbi, Krupp U. Influence of plastic deformation in fatigue crack behavior in bainitic steel. Int J Fatigue 2021;143:106014. https://doi.org/10.1016/j.ijfatigue.2020.106014

[6] Archie F, Zaefferer S. Prior austenite grain boundaries in lath martensite: correlation between the crystallographic character and the fracture susceptibility. Proc 5th Int Symp Steel Sci 2017.

[7] Zhang K, Tang D, Wu H bin. Effect of Heating Rate Before Tempering on Reversed Austenite in Fe-9Ni-C Alloy. J Iron Steel Res Int 2012;19:73–8. https://doi.org/10.1016/S1006-706X(13)60011-4

[8] Syn CK, Fultz B, Morris JW. Mechanical stability of retained austenite in tempered 9Ni steel. Metall Trans A 1978. https://doi.org/10.1007/BF02661946

[9] Choi HJ, Schwartz LH. Fatigue crack propagation in intercritically tempered Fe-9Ni-0.1C and Fe-4Mn-0.15C. Metall Trans A 1983;14:1089–99. https://doi.org/10.1007/BF02670447

[10] Nakanishi D, Kawabata T, Aihara S. Effect of dispersed retained γ-Fe on brittle crack arrest toughness in 9% Ni steel in cryogenic temperatures. Mater Sci Eng A 2018. https://doi.org/10.1016/j.msea.2018.03.056

[11] Zhao XQ, Pan T, Wang QF, Su H, Yang CF, Yang QX, et al. Effect of Intercritical Quenching on Reversed Austenite Formation and Cryogenic Toughness in QLT-Processed 9% Ni Steel. J Iron Steel Res Int 2007;14:240–4. https://doi.org/10.1016/S1006-706X(08)60086-2

[12] Zhang JM, Li H, Yang F, Chi Q, Ji LK, Feng YR. Effect of heat treatment process on mechanical properties and microstructure of a 9% ni steel for large LNG storage tanks. J Mater Eng Perform 2013;22:3867–71. https://doi.org/10.1007/s11665-013-0701-1

[13] G. Jahrsengene1, M. Wenn1, M. Karlsen1, 2, I. Westermann1, O.M. Akselsen1, 3 JH. EBSD quantification of retained austenite in 9% Ni steel related to thermal treatments. The Twenty-fifth International Ocean and Polar Engineering Conference, Kona, Hawaii, USA, 21-26 June 2015. ISBN: 978-1-880653-89-0

[14] Polák J, Sauzay M. Growth of extrusions in localized cyclic plastic straining. Mater

Sci Eng A 2009;500:122–9. https://doi.org/10.1016/j.msea.2008.09.022

[15] Seidametova G, Vogt JB, Proriol Serre I. The early stage of fatigue crack initiation in a 12%Cr martensitic steel. Int J Fatigue 2018;106:38–48. https://doi.org/10.1016/j.ijfatigue.2017.09.006

[16] Cullity BD. Elements of X-ray Diffraction. Addison-Wesley Publishing; 1956.

[17] Chen Y, Hjelen J, Gireesh SS, Roven HJ. Optimization of EBSD parameters for ultra-fast characterization. J Microsc 2012;245:111–8. https://doi.org/10.1111/j.1365-2818.2011.03551.x

[18] Kamaya M. Characterization of microstructural damage due to low-cycle fatigue by EBSD observation. Mater Charact 2009;60:1454–62. https://doi.org/10.1016/j.matchar.2009.07.003

[19] Schayes C, Bouquerel J, Vogt, JB, palleschi F, Zaefferer S. A comparison of EBSD based strain indicators for the study of Fe-3Si steel subjected to cyclic loading. Mater. Charac. 2016;115:61-70. https://doi.org/10.1016/j.matchar.2016.03.020

[20] Zaefferer S, Elhami NN. Theory and application of electron channelling contrast imaging under controlled diffraction conditions. Acta Mater 2014;75:20–50. https://doi.org/10.1016/j.actamat.2014.04.018

[21] Nyyssönen T, Peura P, Kuokkala VT. Crystallography, Morphology, and Martensite Transformation of Prior Austenite in Intercritically Annealed High-Aluminum Steel. Metall Mater Trans A Phys Metall Mater Sci 2018;49:6426–41. https://doi.org/10.1007/s11661-018-4904-9

[22] Maresca F, Kouznetsova VG, Geers MGD. On the role of interlath retained austenite in the deformation of lath martensite. Model Simul Mater Sci Eng 2014;22.

https://doi.org/10.1088/0965-0393/22/4/045011

[23] Morito S, Oh-Ishi K, Hono K, Ohba T. Carbon enrichment in retained austenite films in low carbon lath martensite steel. ISIJ Int 2011;51:1200–2. https://doi.org/10.2355/isijinternational.51.1200

[24] Kwon H, Barlat F, Lee M, Chung Y, Uhm S. Influence of tempering temperature on low cycle fatigue of high strength steel. ISIJ Int 2014;54:979–84. https://doi.org/10.2355/isijinternational.54.979

[25] Archie F, Li X, Zaefferer S. Micro-damage initiation in ferrite-martensite DP microstructures: A statistical characterization of crystallographic and chemical parameters. Mater Sci Eng A 2017;701:302–13. https://doi.org/10.1016/j.msea.2017.06.094

[26] Morito S, Yoshida H, Maki T, Huang X. Effect of block size on the strength of lath martensite in low carbon steels. Mater Sci Eng A 2006;438–440:237–40. https://doi.org/10.1016/j.msea.2005.12.048

[27] Miyamoto G, Iwata N, Takayama N, Furuhara T. Mapping the parent austenite orientation reconstructed from the orientation of martensite by EBSD and its application to ausformed martensite. Acta Mater 2010;58:6393–403. https://doi.org/10.1016/j.actamat.2010.08.001

[28] Raabe D. Dislocation and twin substructure evolution during strain hardening of an Fe – 22 wt .% Mn – 0 . 6 wt .% C TWIP steel observed by electron channeling contrast imaging. Acta Mater 2011;59:6449–62. https://doi.org/10.1016/j.actamat.2011.07.009

[29] Noh HS, Kang JH, Kim KM, Kim SJ. The effect of carbon on hydrogen embrittlement in stable Cr-Ni-Mn-N austenitic stainless steels. Corros Sci 2017;124:63–70. https://doi.org/10.1016/j.corsci.2017.05.004

[30] Wan D, Alvaro A, Olden V, Barnoush A. Hydrogen-enhanced fatigue crack growth behaviors in a ferritic Fe-3wt%Si steel studied by fractography and dislocation structure analysis. Int J Hydrogen Energy 2019;44:5030–42. https://doi.org/10.1016/j.ijhydene.2018.12.190

[31] Luo ZC, Huang MX. The role of interstitial carbon atoms on the strain-hardening rate of twinning-induced plasticity steels. Scr Mater 2020;178:264–8. https://doi.org/10.1016/j.scriptamat.2019.11.047

[32] Lee YK. Microstructural evolution during plastic deformation of twinning-induced plasticity steels. Scr Mater 2012;66:1002–6. https://doi.org/10.1016/j.scriptamat.2011.12.016

[33] Kim SD, Park JY, Park SJ, Jang J hoon, Moon J, Ha HY, et al. Direct observation of dislocation plasticity in high-Mn lightweight steel by in-situ TEM. Sci Rep 2019;9:1–13. https://doi.org/10.1038/s41598-019-51586-y

[34] Astafurova EG, Moskvina VA, Maier GG, Gordienko AI, Burlachenko AG, Smirnov AI, et al. Low-temperature tensile ductility by V-alloying of high-nitrogen CrMn and CrNiMn steels: Characterization of deformation microstructure and fracture micromechanisms. Mater Sci Eng A 2019;745:265–78. https://doi.org/10.1016/j.msea.2018.12.107

[35] Hansen N, Jensen DJ. Development of microstructure in FCC metals during cold work. Philos Trans R Soc A Math Phys Eng Sci 1999;357:1447–69. https://doi.org/10.1098/rsta.1999.0384

[36] Michiuchi M, Nambu S, Ishimoto Y, Inoue J, Koseki T. Relationship between local deformation behavior and crystallographic features of as-quenched lath martensite during uniaxial tensile deformation. Acta Mater 2009;57:5283–91. https://doi.org/10.1016/j.actamat.2009.06.021

[37] Polák J, Man J, Obrtlík K. AFM evidence of surface relief formation and models of fatigue crack nucleation. Int J Fatigue 2003;25:1027–36. https://doi.org/10.1016/S0142-1123(03)00114-2

[38] Du C, Hoefnagels JPM, Vaes R, Geers MGD. Plasticity of lath martensite by sliding of substructure boundaries. Scr Mater 2016;120:37–40. https://doi.org/10.1016/j.scriptamat.2016.04.006

[39] Zhang FC, Long XY, Kang J, Cao D, Lv B. Cyclic deformation behaviors of a high strength carbide-free bainitic steel 2016;94:2015–7.

GRAPHICAL ABSTRACT